Journal of CO_2 Utilization 25 (2018) 147–157

Contents lists available at ScienceDirect

Journal of CO_2 Utilization

journal homepage: www.elsevier.com/locate/jcou

Enhanced CO_2 chemisorption at high temperatures via oxygen addition using (Fe, Cu or Ni)-containing sodium cobaltates as solid sorbents

Elizabeth Vera, J. Francisco Gómez-García, Heriberto Pfeiffer*

Laboratorio de Fisicoquímica y Reactividad de Superficies (LaFReS), Instituto de Investigaciones en Materiales, Universidad Nacional Autónoma de México, Circuito exterior s/n, Cd. Universitaria, Del. Coyoacán C.P. 04510, Ciudad de México, Mexico

ARTICLE INFO

Keywords:
Alkaline ceramic
Sodium cobaltate
CO2 chemisorption
Cyclability

ABSTRACT

Sodium cobaltates containing Fe, Cu or Ni were synthesized, characterized and evaluated for CO_2 capture at high temperatures. Initially, $NaCoO_2$ and metal-containing samples were characterized by XRD, XPS, SEM and N_2 adsorption-desorption, where it was probed that Fe, Cu and Ni were partially incorporated into the $NaCoO_2$ structure. All these ceramics were able to trap CO_2, but only Fe-containing sample presented an important CO_2 chemisorption improvement in comparison to the pristine $NaCoO_2$ sample. Based on these results, a second set of samples was prepared and characterized, varying the iron concentration (10, 20 and 30 mol%). Results showed that CO_2 chemisorption was improved by iron addition up to 20 mol%, but higher amounts of iron did not continue enhancing the chemisorption process. Afterwards, the gas flow was modified adding oxygen (P_{CO2} = 0.95 and P_{O2} = 0.05), resulting in higher CO_2 chemisorption efficiencies and kinetics. These analyses were complemented by CO_2 cyclic experiments, where different gas flows were used, analyzing thermal stability and efficiency evolution.

1. Introduction

Since Nakagawa and Ohashi published in 1998 that lithium metazirconate (Li_2ZrO_3) reacts with carbon dioxide (CO_2) at high temperatures [1], different reports have shown that several alkaline-containing ceramics, especially lithium and sodium ones, are able to chemically trap CO_2 in a wide temperature range [2–20]. Moreover, it has been proposed that these ceramics would be used in different bifunctional sorption-catalytic processes, such as the sorption enhanced steam methane reforming (SE-SMR), which involves the catalytic steam methane reforming (SMR) and water-gas shift reaction processes, as well as carbon monoxide or dioxide sorption by a solid sorbent [21–24]. Within this context, the use of alkaline-containing ceramics, where the heteroatom is supposed to present active catalytic properties, is becoming an important issue. For example, sodium cobaltate ($NaCoO_2$) was recently reported as a possible bifunctional ceramic for the CO oxidation and subsequent CO_2 chemical capture, where different cobalt phases are responsible of the catalytic process [25,26].

Based on the importance of having heteroatoms on the crystal structure of alkaline ceramics, the solid solution syntheses have been evaluated [27–32], where the heteroatom can be an alkaline element (for example $Na_{2-x}Li_xZrO_3$) [32] or other metal or metalloid element (for example $NaZr_{1-x}Al_xO_3$) [33]. When these solid solutions are tested as CO_2 captors, in general, most of them improve different physicochemical properties, such as CO_2 capture temperature range, kinetic and efficiency, among others. The improvements observed on solid solutions are attributed to specific modifications in the crystal structure of ceramics or secondary phases formation [5]. Most of crystal structure modifications imply the formation of crystal point defects, which induce better atomic diffusion and release processes [17,20]. On the contrary, formation of different secondary phases usually modifies microstructural and diffusion properties of the external shell [5,7]. For example, $Li_{4+x}(Si_{1-x}Al_x)O_4$ solid solution importantly improved the CO_2 capture temperature range and chemisorption kinetics, in comparison to Li_4SiO_4 [29]. In this case, carbonation process produces Li_2SiO_3 and $LiAlO_2$ as secondary phases, where $LiAlO_2$ has a better lithium diffusion coefficient than Li_2SiO_3, improving the bulk carbonation processes.

In the same way, as it was already mentioned above, $NaCoO_2$ was recently reported as a possible CO_2 and CO captor material [25,26]. CO_2 capture in $NaCoO_2$ presented an efficiency of 55.9% at 700 °C. Moreover, $NaCoO_2$ catalytic activity was evidenced during the CO oxidation and subsequent CO_2 chemisorption. Furthermore, this ceramic has a hexagonal crystal system composed of $(CoO_2)^{1-}$ pillared layers with sodium atoms at the interlayers [25]. This kind of structure should favor the introduction of different heteroatoms, which consequently may modify CO_2 capture and catalytic properties.

* Corresponding author.
E-mail address: pfeiffer@iim.unam.mx (H. Pfeiffer).

https://doi.org/10.1016/j.jcou.2018.03.019
Received 16 January 2018; Received in revised form 12 March 2018; Accepted 22 March 2018
Available online 30 March 2018

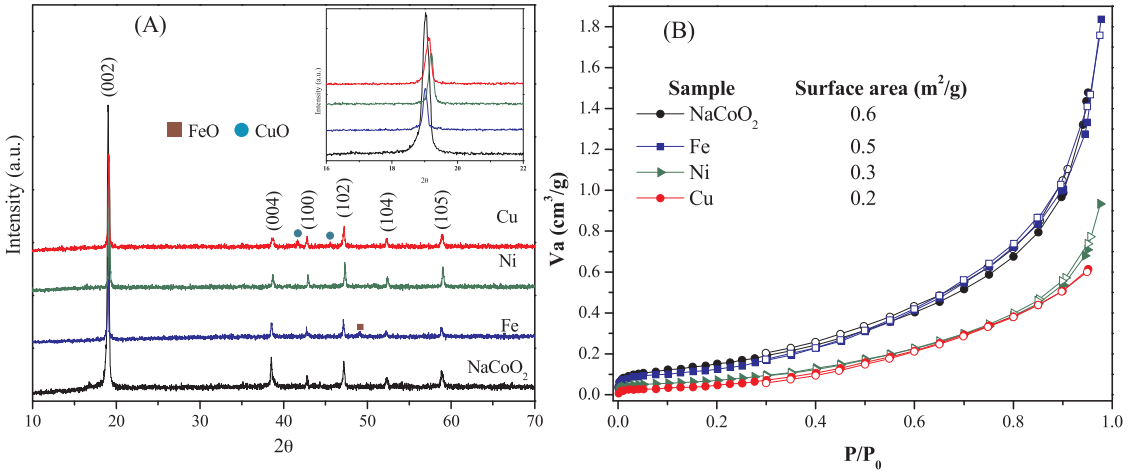

Fig. 1. XRD patterns (A) and N_2 adsorption-desorption isotherms (B) of pristine $NaCoO_2$ and M-$NaCoO_2$ samples (M = Fe, Ni or Cu).

Hence, it has been reported that alkaline ceramics, structural and chemically modified, enhance different CO_2 chemisorption properties, such as kinetics and capture temperature range, among others. Based on that, the aim of this work was to synthesize, characterize and evaluate as CO_2 captors different materials with $NaCo_{1-x}M_xO_2$ chemical composition (M = Cu, Fe or Ni). CO_2 capture process was performed in absence or presence of oxygen. This analysis may be considered an initial step for evaluating other alkaline ceramics as CO_2 captor materials to further utilize them as possible bifunctional catalytic-capture materials in different industrial processes, such as sorption enhanced reforming or H_2 enrichment from syngas flows.

2. Experimental

2.1. Sample synthesis

$NaCo_{1-x}M_xO_2$ (M = Fe, Ni, Cu) samples were synthesized by solid-state reaction method using sodium carbonate (Na_2CO_3, J.T. Baker), cobalt carbonate ($CoCO_3$, Aldrich), iron oxide (Fe_2O_3, MEYER), nickel oxide (NiO) obtained from the calcination of nickel nitrate hexahydrate at 600 °C for 4 h ($Ni(NO_3)_2{\cdot}6H_2O$, Aldrich) or copper oxide (CuO, Sigma Aldrich), adding 27 wt% excess of sodium carbonate to compensate the sublimation effect [33–35]. The corresponding stoichiometric amounts were mixed and calcined at 850 °C for 12 h, adding metallic heteroatom mole contents of x = 0.1 for Ni and Cu, while for Fe the mole content varied between 0.1 and 0.3. $NaCoO_2$ was also synthesized for comparison purposes.

2.2. Characterization techniques

All samples were characterized by powder X-ray diffraction (XRD), nitrogen (N_2) adsorption-desorption, scanning electron microscopy (SEM) and X-ray photoelectron spectroscopy (XPS). XRD patterns were obtained in a D-5000 Siemens diffractometer coupled to Co-K_α anode working at 34 kV and 30 mA. This radiation was used in order to avoid iron fluorescence. Compounds were identified using the Powder Diffraction File (PDF) database. Then, N_2 (Praxair, grade 4.8) adsorption-desorption isotherms were obtained on a Bel-Japan Minisorp II instrument at 77 K with a multipoint technique. Respective specific surface areas were obtained using the Brunauer-Emmet-Teller (BET) model. Microstructural characterization was complemented by scanning electron microscopy, using an equipment JEOL JMS-7600F. Afterwards, XPS analysis was performed in an ESCA2000 Multilab equipment (VG Microtech, from UK) with UHV system, Al K X-ray (1486.6 eV) and CLAM4 MCD analyser. Sample surface was sputtered for 5 min with 0.33 μA/mm^2 argon ions produced at 4.5 kV. The peak positions on the XPS spectra were referenced to C 1s core-level localized at 285.00 eV. XPS spectra were deconvoluted using SDP v4.1 software. The curve fitting procedure was performed as follows: (i) All spectra were calibrated to C 1s peak at 285.00 eV as carbon is ubiquitous and present on any surface; (ii) the linear method for background subtraction was employed in the binding energy (BE) range; (iii) the Gaussian-Lorentzian ratio was fixed to 0.95 to simulate peak profiles; iv) the asymmetry factor was fixed to 0.2; v) the peak positions for Co^{3+} $2p_{3/2}$ and Co^{3+} $2p_{1/2}$ were obtained from the first fit of data for x = 0 sample and then fixed for following analyses; (vi) the full width at half maximum (FWHM) was initially determined on the original sample and then used as initial parameter and; (vii) the best fit was selected by its minimum χ^2 value.

2.3. CO_2 chemisorption tests

CO_2 chemisorption was evaluated in a thermobalance (Q500HR, from TA Instruments) using dynamic, isothermal and cyclic experiments. Initially, $NaCo_{1-x}M_xO_2$ samples were dynamically heated from 30 to 900 °C (5 °C/min), under different gas flows; CO_2 (60 mL/min) or CO_2-O_2 (57-3 mL/min). For isothermal analyses, samples were heated up to desired temperature (between 200 and 800 °C, each 100 °C), under a N_2 flow (60 mL/min, Praxair grade 4.8). Then the gas flow was switched to CO_2 or CO_2-O_2 for 3 h. Finally, different cyclic experiments were performed at 700 °C. In these cases, sorption steps were produced into CO_2 (60 mL/min) or CO_2-O_2 (57-3 mL/min) for 90 min, while desorptions were produced with N_2 (60 mL/min) or N_2-O_2 (57-3 mL/min). Isothermal and cyclic products were characterized by XRD.

3. Results and discussion

XRD patterns of the synthesized compounds ($NaCo_{0.9}M_{0.1}O_2$, where M = Ni, Cu or Fe) are shown in Fig. 1A. All these diffractograms matched to 01-087-0274 PDF file, which corresponds to $Na_{0.74}CoO_2$ phase, with a hexagonal crystal system. It is well known that sodium cobaltate is a non-stoichiometric phase [36,37]. While XRD pattern identification showed the $Na_{0.74}CoO_2$ phase, the sample was labeled as $NaCoO_2$ in the whole work. It was also observed that samples synthesized with Fe and Cu presented secondary phases; iron (II) oxide (FeO, 99-101-0507 PDF file) and copper (II) oxide (CuO, 01-089-5895 PDF file), respectively. Nevertheless, their intensities were very low compared to $NaCoO_2$. The square inset in Fig. 1A presents the XRD reflections corresponding to plane (0 0 2), located at 19.03° for $NaCoO_2$ and $NaCo_{0.9}M_{0.1}O_2$ samples. Fe-containing $NaCoO_2$ sample presented a negligible shift (0.03°), as expected, since both Co^{3+} and Fe^{3+} cations possess the same oxidation state and ionic radius (0.55 Å). On the other hand, samples with Ni and

Cu presented shifts to 19.2 and 19.12°, respectively, indicating that $NaCoO_2$ cell is shrinking. This behavior was not expected, since Ni^{2+} (0.69 Å) and Cu^{2+} (0.73 Å) ionic radii are larger than Co^{3+}. Sodium cobaltate unit cell should expand, although it is important to consider the different oxidation states of doping ions. In this case, for each two incorporated Ni or Cu ions, an oxygen must be released to compensate charge differences. Oxygen ionic radius is 1.35 Å, thus, while lattice tends to expand when adding larger ions, the loss of oxygen counteracts this effect and then lattice tends to shrink, as a larger ion is released. Thus, XRD peak shifts observed are associated to charge compensation caused by oxygen losses. Reactions (1)–(3) represent the changes in each $NaCo_{0.9}M_{0.1}O_2$ arrangement using the Kröger-Vink notation (oxygen contents will be further discussed below).

$$NaCoO_2 \xrightarrow{Fe_2O_3} Na(Co_{1-x}Fe_x)O_2 \rightarrow Na_{Na} + Co_{Co} + Fe_{Co} + O_O \quad (1)$$

$$NaCoO_2 \xrightarrow{2NiO} Na(Co_{1-x}Ni_x)O_2 \rightarrow Na_{Na} + Co_{Co} + 2Ni'_{Co} + O_O + V_{\ddot{O}} \quad (2)$$

$$NaCoO_2 \xrightarrow{2CuO} Na(Co_{1-x}Cu_x)O_2 \rightarrow Na_{Na} + Co_{Co} + 2Cu'_{Co} + O_O + V_{\ddot{O}} \quad (3)$$

The N_2 adsorption-desorption curves are shown in Fig. 1B. All these curves corresponded to isotherms type II according to the IUPAC classification [38], where none of them presented any hysteresis. These features are associated to non-porous or macroporous materials, which is in good agreement with the synthesis method utilized. The specific surface areas were estimated using the BET model, obtaining 0.6, 0.5, 0.3 and 0.2 m^2/g for pristine $NaCoO_2$ and samples containing Fe, Ni or Cu, respectively. As it can be seen, the addition of different metals to $NaCoO_2$ did not modified the textural properties, as the N_2 adsorption-desorption isotherms and BET specific surfaces area did not change importantly. In addition, Fig. 2 shows sample morphological evolution for Fe, Ni or Cu containing samples, with respect to $NaCoO_2$. Initially, secondary electron image of sodium cobaltate shows well-defined polyhedral flake-like particles (Fig. 2A), varying in size from 2 to 8 µm, with 100–300 nm of thickness. In fact, flake-like particles tend to produce non-dense large agglomerates. This morphology is in good agreement with previous reports [25]. However, the addition of transition metals tended to modify $NaCoO_2$ particle morphology and size. Fe-addition presented a similar flake-like morphology (Fig. 2B), but in this case, particle size changed to a bimodal distribution. While

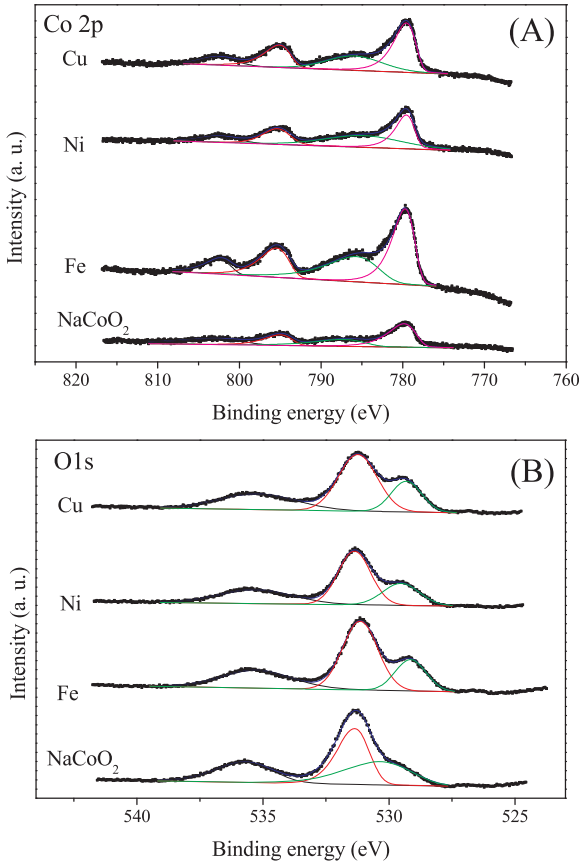

Fig. 3. XPS spectra of Co 2p (A) and O 1s (B) peaks for pristine $NaCoO_2$ and M-$NaCoO_2$ samples (M = Fe, Ni or Cu).

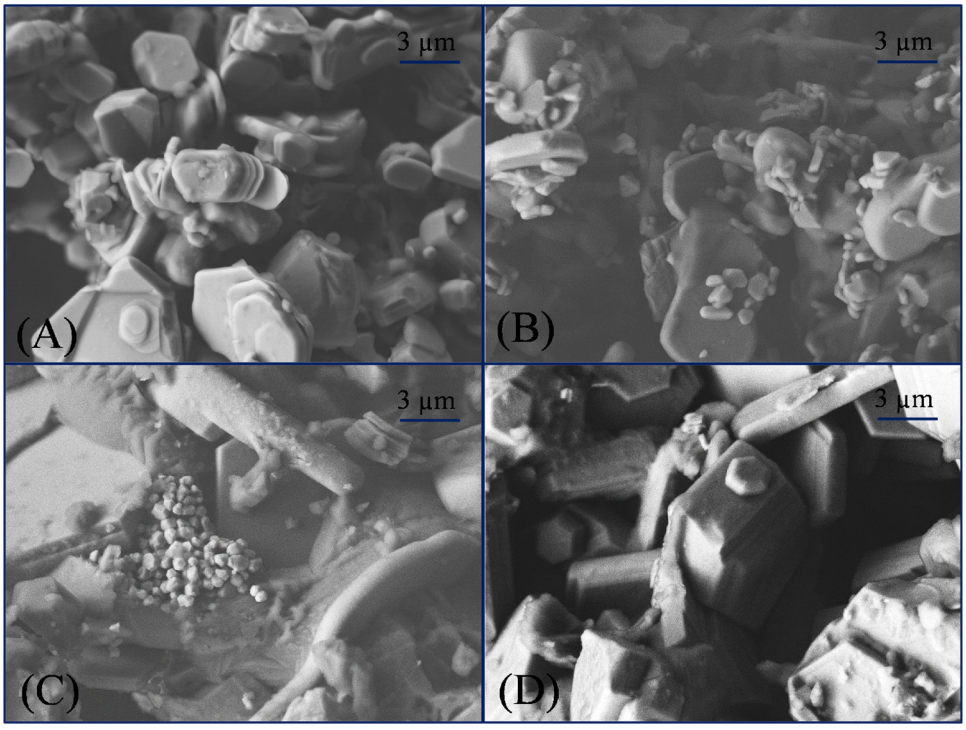

Fig. 2. Secondary electron microscopy images of pristine Na_2CoO_2 (A), Fe-$NaCoO_2$ (B), Ni-$NaCoO_2$ (C) and Cu-$NaCoO_2$ (D) samples.

Table 1
XPS peak positions for Co 2p, and O 1s signals in $NaCoO_2$ and $NaCo_{0.9}M_{0.1}O_2$ samples.

Compound	XPS peak position (eV)				
	Co 2p		O 1s		
	3/2	½	A	B	C
$NaCoO_2$	779.85	795.02	535.71	531.37	530.35
Fe-$NaCoO_2$	779.54	795.46	535.24	531.14	529.14
Ni-$NaCoO_2$	779.57	795.44	535.28	531.37	529.52
Cu-$NaCoO_2$	779.57	795.16	535.21	531.24	529.31

some particles were 2–8 μm size, there was a second set of particles with sizes of ~1 μm. On the contrary, Ni and Cu-containing samples (Fig. 2C and D) morphology presented larger particles and denser agglomerates. This morphological evolution is in good agreement with specific surface areas determined for these samples, where Ni and Cu have slightly lower specific surface areas due to particle growth and densification.

To further analyze the surface and the influence of different cations on $NaCoO_2$, XPS analysis was performed. Fig. 3A shows the deconvoluted Co 2p XPS spectra of pristine $NaCoO_2$ and $NaCo_{0.9}M_{0.1}O_2$ compounds. Pristine $NaCoO_2$ showed characteristic Co^{3+} $2p_{3/2}$ and Co^{3+} $2p_{1/2}$ peaks at 779.85 and 795.02 eV, respectively (Table 1). Peaks located at 785 and 803 eV were associated to satellite peaks. These peaks are present in all $NaCo_{0.9}M_{0.1}O_2$ compounds with similar values, indicating that Co^{3+} binding energy is not affected by Fe^{3+}, Ni^{2+} or Cu^{2+} addition. On the other hand, Fig. 3B displays deconvoluted O 1s XPS spectra for the same samples. All compounds showed three peaks labeled as A–C in the Table 1. In each compound, the highest binding energy values are present in peak A. This peak corresponds to a highly covalent character of O bonds, which can be associated to hydroxyl species or C—O bonds [39]. Additionally, pristine $NaCoO_2$ displayed a prominent peak, labeled as B, at 531.37 eV associated with Co—O bond. Peak C, at 530.35 eV, was associated to a Co—O satellite peak. $NaCo_{0.9}M_{0.1}O_2$ samples displayed similar values for peaks B, indicating that Co—O binding energy is not affected by dopants. Nevertheless, the peaks labeled as C shifted to slightly lower energy values in doped compounds than that of pristine $NaCoO_2$, which implies that dopants are situated, preferably, at the surface of each material, where electrons lose energy, appearing as satellite signals.

Although, the strongest feature of $NaCoO_2$ is its capacity to work as bifunctional material in conversion reactions, the CO_2 chemisorption is a crucial step of the whole process. Therefore, CO_2 capture improvement may as well improve its catalytic behavior if it is doped with adequate transition metals. Based on that, CO_2 chemisorption was evaluated on pristine $NaCoO_2$ and M-$NaCoO_2$ compounds. According with previous studies [25,26], reaction between $NaCoO_2$ and CO_2 leads to produce sodium carbonate (Na_2CO_3) and cobalt oxides, whose composition varies on time. In the case of M-$NaCoO_2$ samples, the formation of each corresponding oxide M_xO_y (M = Fe, Ni or Cu) is also expected. Reactions (4)–(7) show the ideal carbonation process for pristine $NaCoO_2$ and the metal-containing compounds.

$$2\ NaCoO_2 + CO_2 \rightarrow Na_2CO_3 + Co_2O_3 \quad (4)$$

$$2\ NaCo_{1-x}Fe_xO_2 + CO_2 \rightarrow Na_2CO_3 + (1\text{-}x)\ Co_2O_3 + x\ Fe_2O_3 \quad (5)$$

$$2\ NaCo_{1-x}Ni_xO_2 + CO_2 \rightarrow Na_2CO_3 + (1\text{-}x)\ Co_2O_3 + x\ Ni_2O_3 \quad (6)$$

$$2\ NaCo_{1-x}Cu_xO_2 + CO_2 \rightarrow Na_2CO_3 + (1\text{-}x)\ Co_2O_3 + 2x\ CuO + ½x\ O_2 \quad (7)$$

Fig. 4 presents the dynamic TG analysis of $NaCoO_2$ and metal-containing samples in a saturated CO_2 flow (60 mL/min), where it can be seen that all these thermograms exhibited a similar behavior. Initially, thermograms presented a continuous weight increase between

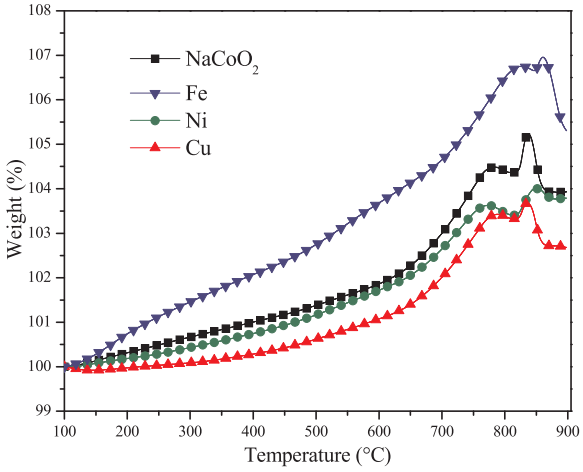

Fig. 4. $NaCoO_2$ and M-$NaCoO_2$ dynamic thermograms on CO_2 flow.

100 °C until decarbonation temperature. Pristine $NaCoO_2$ as well as Ni and Cu containing samples increase their weight in two steps. Between 100 and 650 °C, weight increment was associated with a superficial CO_2 chemisorption, while at higher temperatures, weight increment was associated with bulk chemisorption [10,13]. It could be also observed that decarbonation process was shifted from 840 °C in $NaCoO_2$ to 835 and 850 °C for Cu and Ni-$NaCoO_2$ samples, respectively. Besides, in the whole temperature range CO_2 chemisorption was always larger for $NaCoO_2$. In the Fe-$NaCoO_2$ case, weight increase could be divided in three steps, between 100 to 460 °C, then from 460 to 700 °C and finally from 700 to 860 °C, gaining 2.4, 2.2 and 2.3 wt%, respectively. The first and second steps can be associated to superficial and bulk chemisorption, respectively. Final weight increment, between 700 and 860 °C, can still be considered as a part of bulk chemisorption process, enhanced from a partial iron reduction, where oxygen should be released. These changes are not observed in none of the other samples, where there is no apparent change below 650 °C, where CO_2 volumetric chemisorption begins. This behavior may be associated with different oxidation state of cations, since iron can present more oxidation states. Thus, even the partial presence of FeO on Fe-$NaCoO_2$ samples may enhance CO_2 chemisorption process, as FeO may act as oxygen donor, with the consequent iron reduction.

According to these thermogravimetric results, only iron enhances CO_2 capture, in comparison to pristine $NaCoO_2$. Therefore, different Na$(Co_{1-x}Fe_x)O_2$ compounds were synthesized, with x values between 0.1 to 0.3 in order to analyze the effect of iron content on CO_2 chemisorption. These samples were labeled as Fe10, Fe20 and Fe30, accordingly to iron content in mole percentage. Fig. 5 presents the XRD patterns of Na$(Co_{1-x}Fe_x)O_2$ samples and $NaCoO_2$ as reference. All these diffractograms were identified according to 01-087-0284 PDF file, corresponding to $Na_{0.74}CoO_2$ and none of them presented 2θ shifts. As mentioned before, Fe10 sample presented FeO (99-101-0507 PDF) as a minor secondary phase. In Fe20 sample, a sodium ferrite phase ($NaFeO_2$, 01-076-2299 PDF) appeared. Both, FeO and $NaFeO_2$ tended to increase as a function of iron content, as it could be expected, indicating that iron was not completely incorporated into $NaCoO_2$ crystal structure, by means of a solid-state synthesis.

After the structural characterization, XPS analysis was performed on Fe-$NaCoO_2$ samples. From XPS data (Table 2). it is possible to observe that Co^{3+} $2p_{3/2}$ signal appeared between 779.22 eV and 779.85 eV. This slight fluctuation indicates a negligible influence of Fe^{3+} on Co^{3+} binding energy. Similar behavior was observed in the Co^{3+} $2p_{1/2}$ signal values. Additionally, Fe^{3+} $2p_{3/2}$ and Fe^{3+} $2p_{1/2}$ signal values varied more than Co analogous signals, but these fluctuations are within accepted values for Fe^{3+} signals [40,41]. Fig. 6 shows deconvoluted O 1s XPS spectra of pristine $NaCoO_2$ and Na$(Co_{1-x}Fe_x)O_2$ compounds, where

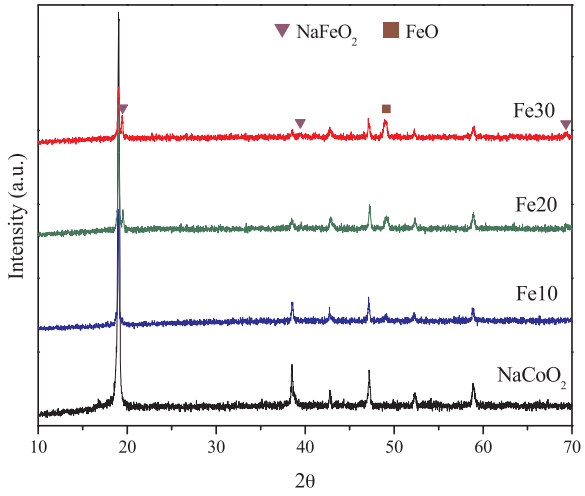

Fig. 5. XRD patterns of Fe-$NaCoO_2$ samples with different iron amounts; 10, 20 and 30 mol%. $NaCoO_2$ XRD pattern is shown for comparison purposes.

Table 2
XPS peak positions for Co 2p, O 1s and Fe 2p signals in iron containing $NaCoO_2$ samples.

Compound	XPS peak position (eV)						
	Co 2p		O 1s			Fe 2p	
	3/2	½	A	B	C	3/2	1/2
$NaCoO_2$	779.85	795.02	535.71	531.37	530.35	–	–
Fe10-$NaCoO_2$	779.54	795.46	535.24	531.14	529.14	710.86	720.91
Fe20-$NaCoO_2$	779.72	795.46	534.79	531.13	529.28	711.02	722.31
Fe30-$NaCoO_2$	779.22	794.98	535.02	530.88	528.74	709.82	723.65

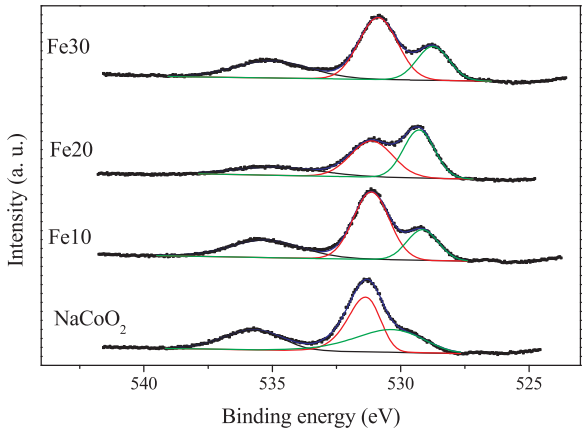

Fig. 6. XPS spectra of O 1s signal for pristine and Fe-containing $NaCoO_2$ sample.

as it was previously described, XPS spectra showed three different signals. Here, it can be observed that the intensity of peak C changed as a function of iron content. In Fe10 sample the peak C intensity is half of the peak B, while in Fe20 sample the intensity of peak C was higher than that of peak B. Peak C enhancement suggests that Fe concentration is mainly located at particle surface. However, in Fe30 sample this peak diminishes again to a similar intensity than that of Fe10 sample. It seems that iron was incorporated to $NaCoO_2$ structure in a higher concentration, which is in good agreement with the peak B shift, which is situated at 531.13 eV for Fe10 and Fe20 samples and at 530.88 eV for Fe30 sample (Table 2).

The dynamic TG analyses of the CO_2 capture on Fe-$NaCoO_2$ samples

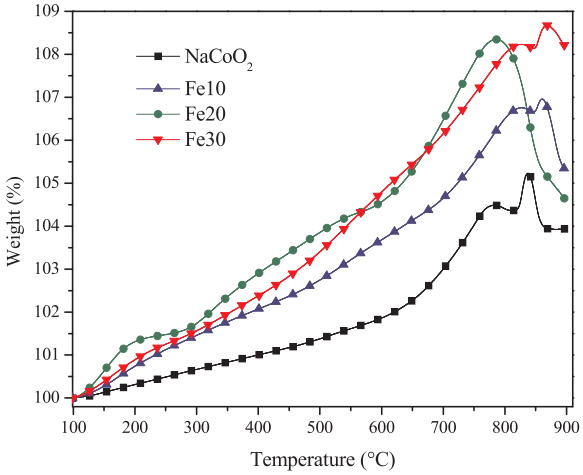

Fig. 7. Dynamic thermograms on CO_2 for Fe-$NaCoO_2$ samples. $NaCoO_2$ thermogram was included for comparison purposes.

are shown in Fig. 7. $NaCoO_2$ dynamic analysis is also shown for comparison purposes. Fe-$NaCoO_2$ samples presented higher CO_2 captures than $NaCoO_2$, in the whole experimental temperature range. As it was mentioned, these samples presented a continuous weight increase that could be divided in three processes. These processes were particularly visible in Fe20 sample: (1) from 100 to 290 °C corresponding to superficial CO_2 chemisorption, (2) from 290 to 600 °C which is bulk chemisorption and (3) from 600 to 790 still corresponding to bulk chemisorption but enhanced by oxygen release caused by iron reduction. These processes, along with decarbonation, were shifted to higher temperatures in Fe10 and Fe30 samples. The slopes of weight increases, corresponding to bulk chemisorption, were also different; 0.0189, 0.0182 and 0.0234 wt%/°C for Fe10, Fe20 and Fe30, respectively. This result suggests that CO_2 chemisorption kinetics is faster in Fe30 sample. In fact, while final weight increased as a function of iron content, it is important to note that Fe20 sample had higher weight increments in almost the whole temperature range. These results are in good agreement with XPS analyses previously mentioned, where it was observed that Fe20 oxygen ions have a different chemical environment than $NaCoO_2$ and other metal-containing samples, as most of iron is located at the particle surface. Therefore, different isothermal experiments were performed using Fe20 sample as CO_2 captor. The obtained products were analyzed by XRD to elucidate the reaction mechanism.

Fig. 8A shows the Fe20 isotherms performed at different temperatures into a CO_2 flow. The first isothermal experiment, performed at 200 °C, exhibited an exponential behavior that had a final weight increment of 2.7 wt% and it did not reach equilibrium after three hours. The consecutive isothermal analysis, performed between 300 and 700 °C, exhibited the same exponential behavior, where final weight increments increased as a function of temperature, from 3.6 wt% at 300 °C to 10.6 wt% at 700 °C, respectively. It has to be mentioned that none of these isotherms achieved equilibrium after three hours. Finally, isotherm performed at 800 °C exhibited an initial weight increase of 9.4 wt% during the first minutes of experiment, then it presented a partial CO_2 desorption. Thus, at T > 700 °C CO_2 chemisorption-desorption equilibrium is modified.

To elucidate the reaction mechanism between CO_2 and Fe20 isothermal products were characterized by XRD, which are presented in Fig. 8B. In the 200 °C isothermal product it was observed that intensity of XRD pattern corresponding to $Na_{0.74}CoO_2$ was reduced, which can be associated to loss of crystallinity. Besides, reflection corresponding to (002) plane, located at 19.03°, was shifted to lower angles. This behavior has been associated to a partial release of sodium from the crystalline cell [25]. The following XRD patterns (300-600 °C) exhibited the formation and gradual increase of Na_2CO_3 and cobalt oxide (Co_3O_4),

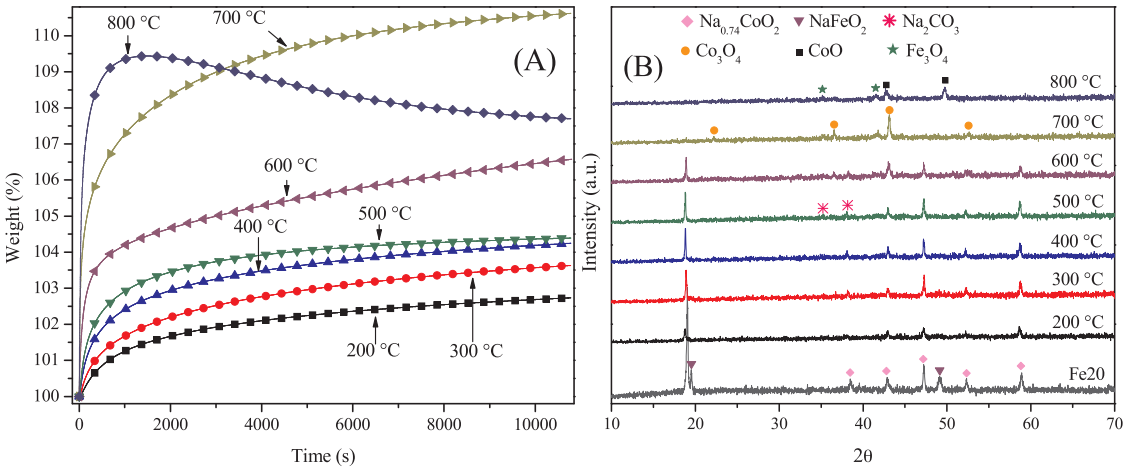

Fig. 8. CO_2 chemisorption isothermal analyses of Fe20 sample at different temperatures (A) and XRD patterns of corresponding products (B).

while $Na_{0.74}CoO_2$ phase remained constant (it did not seem to disappear). At T ≥ 700 °C $Na_{0.74}CoO_2$ phase was no longer present on the diffraction patterns, and additionally, the formation of iron oxide (Fe_3O_4) was observed. Finally, at 800 °C a different cobalt oxide was formed (CoO). XRD results evidenced that cobalt and iron metals change their oxidation state during carbonation. Cobalt was reduced from Co^{3+} to Co^{2+} (Reaction (8)), while iron was partially reduced from Fe^{3+} to Fe^{2+} (Reaction (9)). Of course, these metallic reduction process must be accompanied with an oxidation process; the oxygen lattice release. Based on that, the corresponding reaction mechanism is proposed for $Na_{0.74}(Co_{0.8}Fe_{0.2})O_2$ carbonation process (Reaction (10), where cobalt and iron oxides evolutions were previously described in the Reactions (8) and (9)).

$$3Co_2O_3 \xrightarrow{300-700\,^{\circ}C} 2Co_3O_4 + \frac{1}{2}O_2 \xrightarrow{T>700^{\circ}C} 6CoO + \frac{3}{2}O_2 \quad (8)$$

$$3Fe_2O_3 \xrightarrow{T\geq 600^{\circ}C} 2Fe_3O_4 + \frac{1}{2}O_2 \quad (9)$$

$$Na_{0.74}(Co_{0.8}Fe_{0.2})O_2 + \left(\frac{0.74}{2}\right)CO_2 \rightarrow \left(\frac{0.74}{2}\right)Na_2CO_3 + (0.8)\,\text{Co oxides}_{(Rx-8)} + (0.2)\,\text{Fe oxides}_{(Rx-9)} \quad (10)$$

As it was mentioned, Co and Fe reductions lead to oxygen release, enhancing CO_2 chemisorption by making bulk chemisorption process less dependent on oxygen crystalline diffusion through $NaCoO_2$ crystalline cell [42]. It also seems that iron addition modifies cobalt reduction mechanism, since it takes place at higher temperatures than in $NaCoO_2$ [25]. According to this reaction mechanism, the highest chemisorption efficiency reached in the isothermal analyses was 69.9%, at 700 °C, which is larger than that of $NaCoO_2$ at the same temperature (55.9%).

Although Fe containing $NaCoO_2$ sample presented the best CO_2 chemisorption properties, similar analyses were performed on Cu- and Ni-$NaCoO_2$ samples to compare the CO_2 capture among them. Fig. 9 shows the final weight increments of these isothermal analyses. Trends observed for all samples were similar, where the maximum weight gained increased as a function of temperature, from 500 to 700 °C. At 800 °C, CO_2 chemisorption-desorption equilibrium was modified towards decarbonation, independently of the cation used. Similar to dynamic analyses (Fig. 5), Fe20 sample has a greater weight increment in the whole temperature range compared to other samples. The maximum weight increment in all samples is observed at 700 °C, where it varied from 6.1 wt% in Ni-$NaCoO_2$ to 10.6 wt% in Fe20. Since all these samples have similar surface areas, differences in CO_2 chemisorption are merely dependent on metal addition; Ni, Cu or Fe. Differences

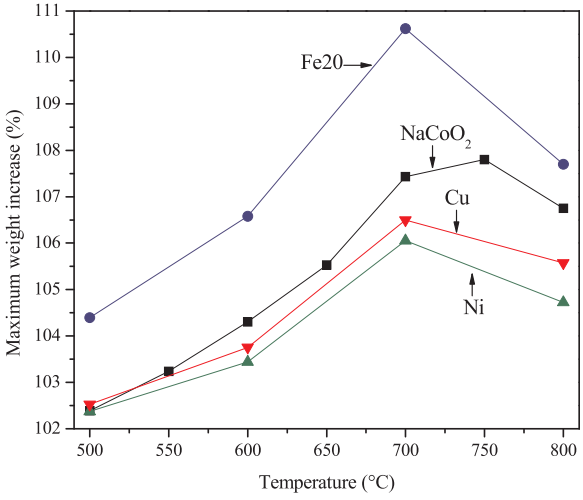

Fig. 9. Comparison of maximum weight increments of isothermal analyses at different temperatures for $NaCoO_2$ and M-$NaCoO_2$ (M = Fe, Ni or Cu) samples.

observed may be related to structural and chemical variations produced during cation additions. Iron presents the same oxidation state than cobalt, 3 + . Conversely, copper and nickel have lower oxidation states (2+), which produced structural changes (described in the Krögen-Vink Reactions (2) and (3)). Moreover, $M \underset{\delta_1}{-} O \underset{\delta_2}{-} Na$ (where M = Co, Fe, Cu or Ni) bonding charge densities change as a function of cation as follows; $Ni \underset{\delta}{-} O < Cu \underset{\delta}{-} O < Co \underset{\delta}{-} O < Fe \underset{\delta}{-} O$ due to electronegativity and oxidation state values. The $O \underset{\delta_2}{-} Na$ bound charge density is increased by Cu and Ni addition, but decreased by Fe addition on $NaCoO_2$. Therefore, Fe-$NaCoO_2$ samples have a larger oxygen availability to be released and sodium atom mobility during CO_2 chemisorption process than Ni- or Cu-$NaCoO_2$ samples, which are already oxygen deficient structures and where sodium atoms are strongly bounded.

To complement the isothermal analysis of Fe20 sample, a kinetic analysis was performed. As there are several processes involved during CO_2 capture, namely, superficial and bulk chemisorption as well as Co and Fe reduction, data was fitted to a first order reaction during the first moments of reaction. In this short time section, it can be assumed that the sole reaction taking place is related to Fe20 particles and CO_2, assuming a saturated atmosphere (60 mL/min). Therefore, the equation corresponding to rate of reaction can be written as:

$$\ln[Na_{0.74}(Co_{0.8}Fe_{0.2})O_2] = -kt \quad (11)$$

where, $[Na_{0.74}(Co_{0.8}Fe_{0.2})O_2]$ is the sample concentration, k is the

Table 3
Rate constants values (k) obtained for Fe20-$NaCoO_2$ sample from the first order reaction model, using CO_2 on the gas flow.

T (°C)	k (1/s)	R^2
200	1.29×10^{-4}	0.9962
300	3.12×10^{-4}	0.9998
400	6.18×10^{-4}	0.9997
500	8.92×10^{-4}	0.9999
600	1.84×10^{-3}	0.9976
700	2.41×10^{-3}	0.9949
800	4.19×10^{-3}	0.9968

reaction rate constant and t is time. Data were only fitted for the first 60 s to consider a superficial reaction. Table 3 shows the obtained k values, which had a linear trend as a function of temperature, varying from 1.2×10^{-4} to $4.2 \times 10^{-3}\,s^{-1}$. Rate constants were fitted to Eyring's model for heterogeneous reactions to calculate the activation enthalpy ($\Delta H^{\ddagger}$) of reaction. Using this model, a $\Delta H^{\ddagger}$ value of 17.9 kJ/mol was obtained.

k and $\Delta H^{\ddagger}$ obtained values are comparable to other values of different Na and Li ceramics. For instance, the rate constant values of Fe20-$NaCoO_2$ and $NaCO_2$ [25] samples were very similar among them (~5–10%), although $\Delta H^{\ddagger}$ values did vary. While $\Delta H^{\ddagger}$ value of $NaCoO_2$ was around 50 kJ/mol (between 400 and 750 °C), Fe20-$NaCoO_2$ reduced its $\Delta H^{\ddagger}$ to 17.9 kJ/mol. This result clearly shows that iron addition to sodium cobaltate reduces its temperature dependence of CO_2 chemisorption process, at least in the first moments of the whole process. Moreover, if k values are compared with Li_5AlO_4 and Li_5FeO_4, which present some of the best CO_2 chemisorption capacities, it can be seen that the corresponding Li_5AlO_4 rate constants oscillate between 7.3×10^{-4} and $7.4 \times 10^{-3}\,s^{-1}$ while Li_5FeO_4 values varied from 1×10^{-3} to $5 \times 10^{-3}\,s^{-1}$ [40]. Thus, k constants obtained with Fe20-$NaCoO_2$ sample have the same order of magnitude. On the other hand, the activation enthalpy value obtained here is considerably low compared to Na_2TiO_3 (188.1 kJ/mol) [14] and Li_5FeO_4 (88.3 kJ/mol) [40], but similar to Na_2ZrO_3 (33 kJ/mol) [43] and $Na_2(Zr_{0.7}Al_{0.3})O_3$ (22–30 kJ/mol) [33]. Based on this comparison, it can be seen that iron-containing $NaCoO_2$ has similar rate constant values than other important alkaline ceramics, but it presents one of the lowest temperature dependence ($\Delta H^{\ddagger}$) during CO_2 chemisorption. Moreover, it has to be mentioned that Fe-containing sodium cobaltate has shown the ability of trapping CO_2 at temperatures as high as 800 °C, which is something not so common on this kind of materials. Besides, it has to be noticed that few alkaline and earth-alkaline ceramics have reported CO_2 chemisorption improvements by the oxygen addition ($P_{O2} \leq 0.2$) [42]. CO_2 chemisorption on sodium containing ceramics not only depends on CO_2 concentration, temperature and pressure, but on the Na^{1+} and O^{2-} diffusion properties over the external shell. In this specific case, sodium atoms have to diffuse from $NaCoO_2$ to Na_2CO_3 and cobalt oxide core shell surface, but some oxygen atoms too. Previously, it was established that CO_2 chemisorption on iron-containing samples was enhanced due to oxygen release caused by metal reduction. Thus, oxygen presence on the gas flow must show a higher CO_2 chemisorption improvement on iron containing samples, than that of pristine $NaCoO_2$. Based on that, different dynamic and isothermal thermograms were performed on $NaCoO_2$ and iron containing samples (Fe10-, Fe20- and Fe30-$NaCoO_2$) with the following gas mixture; P_{CO2}:P_{O2} = 0.95:0.05.

Fig. 10 shows dynamic thermograms of the CO_2 capture, in presence of oxygen, on $NaCoO_2$ and Fe-containing samples. All samples presented continuous weight increments, as those thermograms obtained in absence of oxygen (see Fig. 7), although the following changes must be pointed out. (*i*) Fe-$NaCoO_2$ samples presented higher CO_2 captures than pristine $NaCoO_2$ in the whole temperature range; at superficial (150–300 °C) and bulk (400–800 °C) levels. In fact, weight increment was favored as a function of iron content, where Fe30-$NaCoO_2$ sample

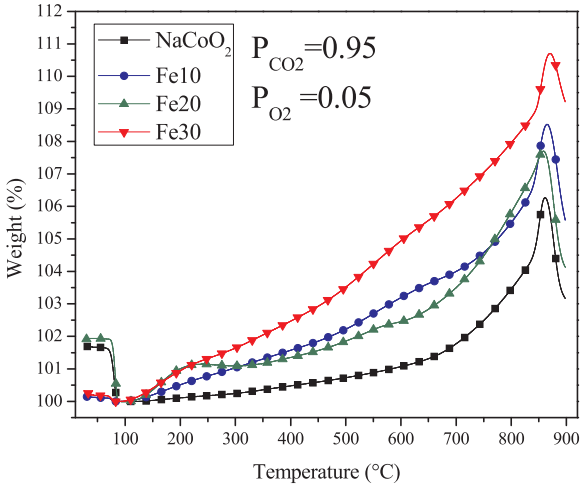

Fig. 10. Dynamic thermograms on CO_2-O_2 (P_{CO2}:P_{O2} = 0.95:0.05) flow for $NaCoO_2$ and Fe-$NaCoO_2$ samples. Weight percentages were normalized at 100 wt% after dehydration process (T = 100 °C).

presented the highest CO_2 chemisorption. (*ii*) Qualitatively, CO_2 chemisorption, in oxygen presence, was always higher than that obtained in oxygen absence, independently of iron content. (*iii*) CO_2 capture segmentation, as a function of temperature, was not so evident. Temperature segmentation had been attributed to iron reduction, which may not occur now, since oxygen was added.

Based on previous results, different isothermal experiments were performed on Fe30-$NaCoO_2$ (sample with the best qualitative performance) in presence of a CO_2:O_2 gas mixture (P_{CO2}:P_{O2} = 0.95:0.05, Fig. 11). At 500 °C, Fe30-$NaCoO_2$ sample gained 6.4 wt%, being the lowest CO_2 chemisorption. At higher temperatures, final weights increased as a function of temperature; 8.5, 10.6 and 12.3 wt% at 600, 700 and 800 °C, respectively. When CO_2 chemisorption was performed in oxygen absence (see Fig. 7) the maximum weight increments were always lower than those obtained with oxygen, except at 700 °C, where both isotherms captured 10.6 wt%. However, while in absence of oxygen this was the best CO_2 chemisorption temperature, CO_2 chemisorption was improved at 800 °C (12.3 wt%) in oxygen presence. Therefore, oxygen addition to gas flow enhances CO_2 chemisorption and thermal stability of carbonation process. Additionally, isothermal data was fitted to first order reaction model to obtain the corresponding k rate constant values (Table 4) and compare them with previous results obtained in oxygen absence (see Table 3). At any temperature, these k

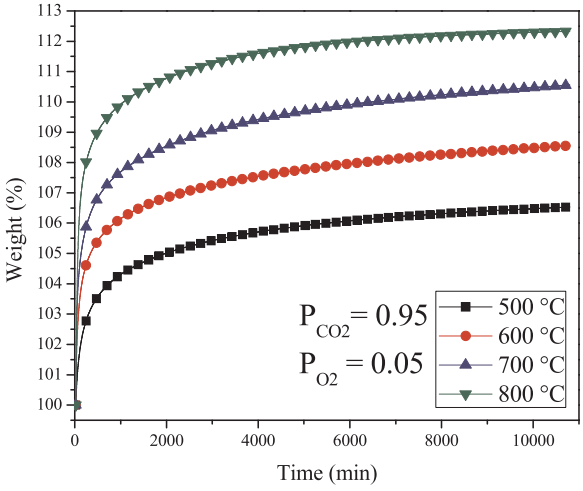

Fig. 11. CO_2 chemisorption isothermal analyses of Fe30-$NaCoO_2$ sample at different temperatures, with specific P_{CO2} and P_{O2}.

Table 4
Rate constants values (k) obtained for Fe30-$NaCoO_2$ sample from the first order reaction model, using CO_2 and O_2 on the gas flow.

T (°C)	k (1/s)	R^2
500	1.78×10^{-3}	0.9958
600	3.04×10^{-3}	0.9944
700	4.86×10^{-3}	0.9756
800	7.87×10^{-3}	0.9986

values indicated faster CO_2 chemisorption in oxygen presence than those in oxygen absence; confirming that oxygen presence improves CO_2 chemisorption and thermal stability. As in the previous case, $\Delta H^{\ddagger}$ value was obtained from the Eyring's equation, obtaining a $\Delta H^{\ddagger}$ value of 26.3 kJ/mol, indicating that oxygen addition increases temperature dependence on whole process, in comparison to the same reaction process in oxygen absence (17.9 kJ/mol).

CO_2-O_2 isothermal products were analyzed by XRD (data not shown), to fully understand the variations produced by oxygen addition on reaction mechanism. XRD patterns obtained from these isothermal products at T ≤ 700 °C evidenced the formation of $Na_{0.74}CoO_2$, Na_2CO_3 and cobalt oxide (Co_3O_4), as sodium and cobalt phases, while Fe_3O_4 was the only iron-containing phase found. Only at 800 °C a different cobalt oxide phase was found, CoO, and $Na_{0.74}CoO_2$ was almost not present on this diffraction pattern. Moreover, as it was described above, metallic reduction is accompanied with oxygen release (oxidation process). Based on these results, oxygen presence must have modified the reaction mechanism as follows, where iron is working as intermediate and catalytic specie. Once oxygen diffusion and release began, iron may be reduced enhancing this process by releasing oxygen to form CO_3^{2-} ions, but at the same time iron acted as catalyst, dissociating oxygen molecules and housing new oxygen atoms. In such a way, iron must perform a triple-process cycle; reducing, oxygen dissociating and oxidizing, as it is schematized on Fig. 12. Cobalt could have a similar oxidation-reduction behavior; however, it is mostly located in the material's bulk (both in pristine and iron containing samples). On the other hand, as XPS results showed, iron is preferably located on the surface of samples, thus allowing a faster oxidation-reduction process, and consequently a faster and improved CO_2 chemisorption. This was confirmed by the kinetic values obtained before. Otherwise, if it were simply assumed that oxygen inhibits iron reduction, the presence of iron would be useless and pristine $NaCoO_2$ sample must had presented the best behavior, which did not happen. Of course, some iron atoms must be gradually reducing and stabilizing (deactivating oxygen interchange) due to the formation of chemisorption products, which explains the Fe_3O_4 formation.

Based on previous comparison and proposal, one of the most important properties to be analyzed corresponds to CO_2 chemisorption-desorption properties. Thus, to evaluate and compare $NaCoO_2$ and Fe20 in cyclic conditions, several sorption-desorption tests were performed (Fig. 13). These experiments were implemented in presence or absence of oxygen during CO_2 desorption step, as there are different papers showing that an oxidant specie, for example O_2 or H_2O, enhance desorption and ceramic regeneration [42,44]. The first set of analyses were carried out by carbonating samples at 700 °C during 90 min in a saturated flow of CO_2. Then, desorption stages were performed at the same temperature by changing the gas flow to only N_2 for 90 min. In both samples, CO_2 capture tended to decrease as a function of cycles, thus gradually reducing the efficiency of these materials. Each cycle tended to decrease exponentially (Fig. 13). This performance can be associated with reaction mechanism between CO_2 and $NaCoO_2$ or Fe20. As previously mentioned, carbonation leads to partial reduction of Co and Fe (in the case of Fe20), which results in oxygen release. While oxygen release enhances CO_2 chemisorption, after several cycles the sample becomes oxygen-deficient, making it less reactive towards CO_2 capture. To overcome this limitation a new set of sorption-desorption cyclic experiments were performed, where oxygen was added during desorption stage to recover the pristine stoichiometry of samples. Fig. 13A presents the cyclic experiments of $NaCoO_2$ and Fe20 in presence of O_2 during desorption. Fe20 presents an initial weight increase of 6.8 wt% with a consecutive weight decrease of 8.6 wt%. This difference may be attributed to previous carbonation of sample. In the last chemisorption cycle, a 5.3 wt% weight increase was achieved. For $NaCoO_2$, the first and last chemisorptions corresponded to weight increases of 6.3 and 5.4 wt%. The cycles performed in O_2 presence during sorption and desorption stages are presented in Fig. 13B. $NaCoO_2$ presented a similar behavior than that of the last experiment, however the loss of efficiency during cycles was slightly lower, passing from a weight increase of 5.7 to 5.3 wt% between first and last cycles. In the Fe20 case, after the third decarbonation process, cycles tended to stabilize in a weight gain of 7.5 wt%, which is a higher CO_2 chemisorption than that obtained in absence of O_2 during carbonation step (5.3 wt%). Therefore, the presence of O_2 affects in two ways the cyclic behavior, (i) enhancing CO_2 chemisorption by aiding the oxidation-reduction cycle of iron and (ii) recovering the pristine sodium cobaltate phase before a new cycle begins.

Fig. 13C presents CO_2 capture efficiencies of all experiments described above. If no oxygen was supplied during desorptions, cycles showed a rapid decrement of sorption efficiency. However, it must be pointed out that Fe20 sample always presents a higher efficiency than

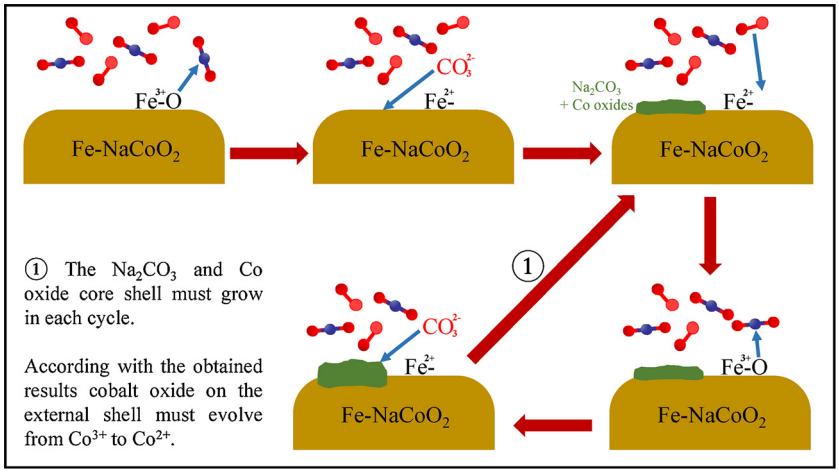

Fig. 12. Schematic representation of oxygen addition effect during CO_2 chemisorption on iron containing $NaCoO_2$ samples, where iron oxidation state changes as a function of oxygen dissociation and release.

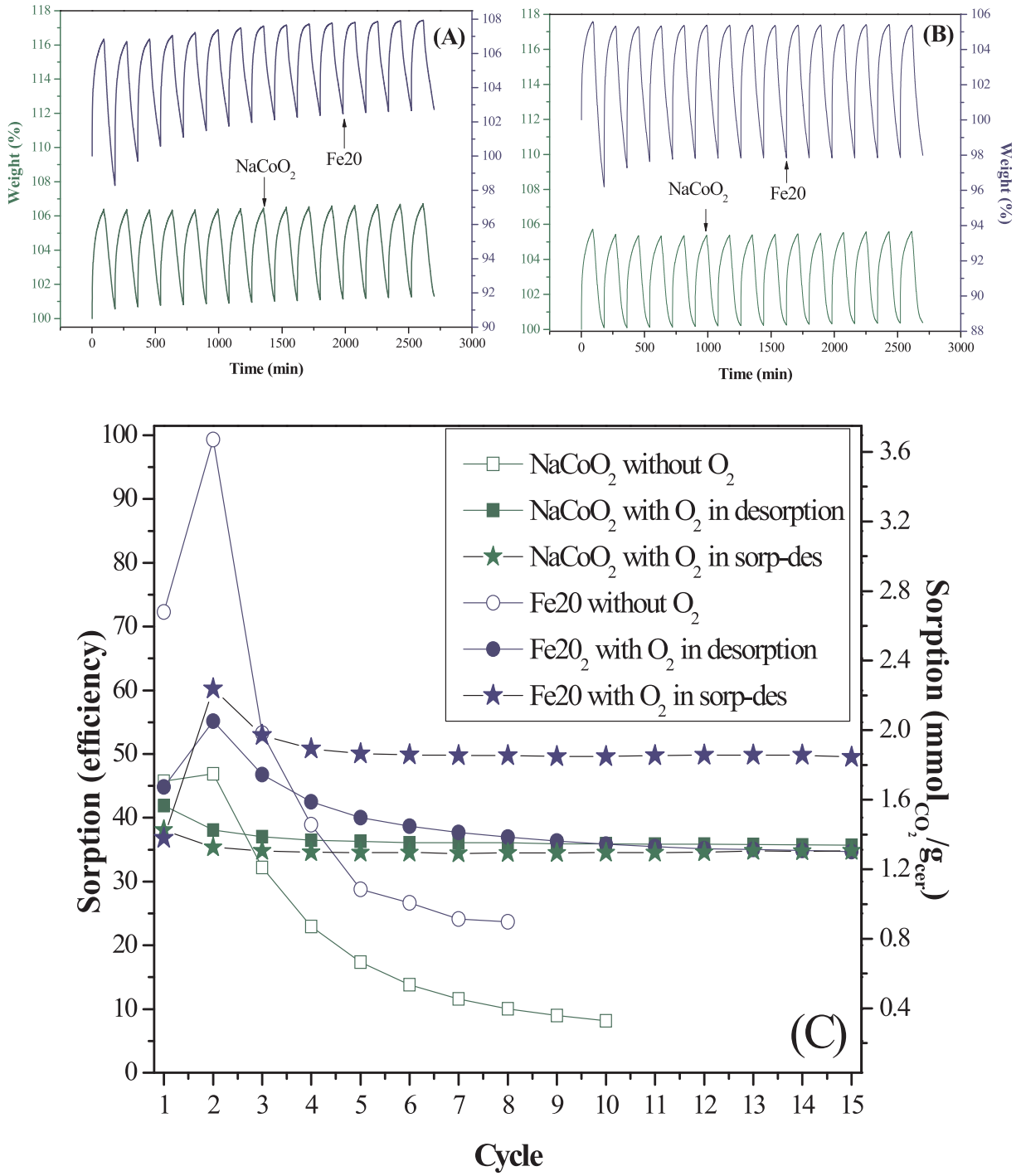

Fig. 13. CO_2 sorption-desorption (700–700 °C) cyclic tests of $NaCoO_2$ and Fe-$NaCoO_2$ performed with addition of oxygen during the sorption and/or desorption steps (A). Comparison of the $NaCoO_2$ and Fe-$NaCoO_2$ stabilities when oxygen was present, or not, during sorption steps (B).

$NaCoO_2$. In addition, this tendency does not seem to be stabilized even after 8 cycles. On the other hand, for cycles performed with oxygen, CO_2 capture tends to stabilize both samples. $NaCoO_2$ stabilizes at around 35% of efficiency (1.4 $mmol_{CO2}/g_{cer}$) on both experiments. In the case of Fe20, cycles performed with O_2 only in desorption, stabilize also at 35% of efficiency, but cycles performed in O_2 during all the experiment present a faster stabilization and greater efficiency, 50% (1.7 $mmol_{CO2}/g_{cer}$). In fact, these data can be adjusted to an exponential regression in order to calculate the minimum efficiency of samples after a large number of cycles. The equation corresponding to the decreasing exponential is:

$$y = A + Be^{-x/t} \quad (12)$$

where y, x, A, B and t correspond to the CO_2 efficiency that can be achieved, the number of cycles, the offset, amplitude and decay constant of the curve, respectively. For cycles without oxygen, the minimum sorption efficiencies are 7.4 and 21.3% for $NaCoO_2$ and Fe, respectively, while for cycles with oxygen during desorption steps, these values are 35.9 and 35.1%, and 34.6 and 49.7% for experiments with O_2 in the whole process, which are in good agreement with these experimental data.

To further analyze cyclic behavior, products of these analyses were characterized by XRD (data not shown). Cycles performed without

oxygen, evidenced Na_2CO_3, CoO and FeO (only in Fe20 sample). It is worth noting that when a single isotherm was performed at equal temperature, only Co_3O_4 and Fe_3O_4 were formed. Thus, performing several sorption-desorption cycles produce a progressive reduction of Fe and Co. On the other hand, products of cycles with oxygen on desorption steps, presented mainly $Na_{0.74}CoO_2$ phase, along with Na_2CO_3, Co_3O_4 and Fe_2O_3 (only in Fe20). Thus, despite some products remain after decarbonation step, pristine sample is regenerated. These results are in good agreement with the behavior observed in cyclic experiments. When oxygen is added to desorption step, compounds regenerate allowing to continue the cyclic CO_2 capture.

4. Conclusions

Pristine $NaCoO_2$ and other samples containing Fe, Cu or Ni (10 mol %) were synthesized by solid-state reaction. All these samples were characterized by structural (XRD) and superficial (XPS, SEM and N_2 adsorption-desorption) techniques. Based on the characterization results, it was determined that Fe, Cu and Ni are only partially incorporated into $NaCoO_2$ structure. The other metal portions are located over the $NaCoO_2$ particle surfaces as metal oxides. After the characterization process, samples were tested on CO_2 chemisorption, through dynamic thermogravimetric experiments. While Fe-containing sample highly improved CO_2 chemisorption, Cu- and Ni-containing samples reduced CO_2 chemisorption, in comparison to pristine $NaCoO_2$ sample. CO_2 chemisorption observed on iron containing sample was attributed to the following factors. Fe presents the same oxidation state than cobalt (3+), in comparison to Cu and Ni (2 +). This fact, in addition to electronegativity values, produced structural changes on $M\ \overline{\delta_1}\ O\ \overline{\delta_2}\ Na$ bound charge densities, as follows; $Ni\ \overline{\delta}\ O < Cu\ \overline{\delta}\ O < Co\ \overline{\delta}\ O < Fe\ \overline{\delta}\ O$. Thus, $O\ \overline{\delta_2}\ Na$ bound charge density is increased on Cu and Ni cases, but decreased on the Fe case.

Based on these results, iron concentration was varied on Fe-$NaCoO_2$ sample (10, 20 and 30 mol%), and they were characterized by the same structural and superficial techniques. Characterization confirmed that only part of iron is located into $NaCoO_2$ structure and the other part formed iron (II) oxide (FeO) and sodium ferrite ($NaFeO_2$), indicating a partial iron reduction. Independently of iron content, Fe-$NaCoO_2$ samples presented a higher CO_2 chemisorption than pristine $NaCoO_2$. CO_2 chemisorption was observed from very low temperatures (~100 °C) to 800 °C. Thus, CO_2 isotherms were performed between 200 and 800 °C (each 100 °C), where carbonation process was confirmed, through CO_2 capture and partial cobalt and iron reductions. Moreover, kinetic parameter values (k) obtained for Fe20-$NaCoO_2$ reaction mechanism increased as a function of temperature, as it could be expected, showing some CO_2 desorption at 800 °C. Besides, $\Delta H^{\ddagger}$ value was determined; 17.9 kJ/mol. Therefore, CO_2 chemisorption dependence on temperature on $NaCoO_2$ is importantly reduced by iron addition, as $\Delta H^{\ddagger}$ of $NaCoO_2$ reported values are 52.8 and 48.8 kJ/mol. Based in all previous results, a second set of Fe-containing $NaCoO_2$ were evaluated modifying the gas flow composition to P_{CO2}:P_{O2} = 0.95:0.05, during CO_2 chemisorption. Results clearly showed that oxygen addition improves kinetics, efficiencies, thermal stability and reaction mechanism of CO_2 chemisorption on Fe-containing $NaCoO_2$ samples. All these changes were attributed to iron reduction-oxidation ability.

Finally, different cyclic experiments were performed on $NaCoO_2$ and Fe20-$NaCoO_2$ samples. Results clearly show that both samples are partially decomposed by oxygen release produced during CO_2 capture. Therefore, in order to avoid sample decomposition, a second set of cycles were performed adding oxygen during desorption step. In these cases, samples were regenerated and cyclic stability was highly improved. Finally, a set of cycles with oxygen during sorption and desorption stages were performed, showing the same stability and regeneration, with an enhancement of CO_2 chemisorption (only in the Fe20 sample) caused by oxidation-reduction cycle of iron.

Acknowledgements

E. Vera and J. F. Gómez-García thank to CONACYT and DGAPA-UNAM for personal financial supports, respectively. The present work was financially supported by project SENER-CONACYT (251801). Finally, authors thank to A. Tejeda and L. Huerta for technical assistance.

References

[1] K. Nakagawa, T. Ohashi, A novel method of CO_2 capture from high temperature gases, J. Electrochem. Soc. 145 (1998) 1344–1347, http://dx.doi.org/10.1149/1.1838462.
[2] L.K.G. Bhatta, S. Subramanyam, M.D. Chengala, S. Olivera, K. Venkatesh, Progress in hydrotalcite like compounds and metal-based oxides for CO_2 capture: a review, J. Clean. Prod. 103 (2015) 171–196, http://dx.doi.org/10.1016/j.jclepro.2014.12.059.
[3] N. Rashidi, S. Yusup, An overview of activated carbons utilization for post-combustion carbon dioxyde capture, J. CO_2 Util. 13 (2016) 1–16, http://dx.doi.org/10.1016/j.jcou.2015.11.002.
[4] J. Wang, L. Huang, R. Yang, Z. Zhang, J. Wu, Y. Gao, Q. Wang, D. O'Hare, Z. Zhong, Recent advances in solid sorbents for CO_2 capture and new development trends, Energy Environ. Sci. 7 (2014) 3478–3518, http://dx.doi.org/10.1039/C4EE01647E.
[5] J. Ortiz-Landeros, T.L. Ávalos-Rendón, C. Gómez-Yáñez, H. Pfeiffer, Analysis and perspectives concerning CO_2 chemisorption on lithium ceramics using thermal analysis, J. Therm. Anal. Calorim. 108 (2012) 647–655, http://dx.doi.org/10.1007/s10973-011-2063-y.
[6] M.T. Dunstan, A. Jain, W. Liu, S.P. Ong, T. Liu, J. Lee, K.A. Persson, S.A. Scott, J.S. Dennis, C.P. Grey, Large scale computational screening and experimental discovery of novel materials for high temperature CO_2 capture, Energy Environ. Sci. 9 (2016) 1346–1360, http://dx.doi.org/10.1039/C5EE03253A.
[7] S. Kumar, S.K. Saxena, A comparative study of CO_2 sorption properties for different oxides, Mater. Renew. Sustain. Energy 3 (2014), http://dx.doi.org/10.1007/s40243-014-0030-9.
[8] F. Bamiduro, G. Ji, A.P. Brown, V.A. Dupont, M. Zhao, S.J. Milne, Spray-dried sodium zirconate: a rapid absorption powder for CO_2 capture with enhanced cyclic stability, ChemSusChem 10 (2017) 2059–2067, http://dx.doi.org/10.1002/cssc.201700046.
[9] A. Nambo, J. He, T.Q. Nguyen, V. Atla, T. Druffel, M. Sunkara, Ultrafast carbon dioxide sorption kinetics using lithium silicate nanowires, Nano Lett. 17 (2017) 3327–3333, http://dx.doi.org/10.1021/acs.nanolett.6b04013.
[10] G. Ji, M.Z. Memon, H. Zhuo, M. Zhao, Experimental study on CO_2 capture mechanisms using Na_2ZrO_3 sorbents synthesized by soft chemistry method, Chem. Eng. J. 313 (2017) 646–654, http://dx.doi.org/10.1016/j.cej.2016.12.103.
[11] K. Wang, W. Li, Z. Yin, Z. Zhou, P. Zhao, High-capacity Li_4SiO_4-based CO_2 sorbents via a facile hydration-NaCl doping technique, Energy Fuels 31 (2017) 6257–6265, http://dx.doi.org/10.1021/acs.energyfuels.6b03453.
[12] H. Takasu, J. Ryu, Y. Kato, Application of lithium orthosilicate for high-temperature thermochemical energy storage, Appl. Energy 193 (2017) 74–83, http://dx.doi.org/10.1016/j.apenergy.2017.02.029.
[13] I. Ham-Liu, J.A. Mendonza-Nieto, H. Pfeiffer, CO_2 chemisroption enhancement produced by K_2CO_3- and Na_2CO_3-addition on Li_2CuO_2, J. CO_2 Util. 23 (2018) 143–151, http://dx.doi.org/10.1016/j.jcou.2017.11.009.
[14] P. Sánchez-Camacho, I.C. Romero-Ibarra, Y. Duan, H. Pfeiffer, Thermodynamic and kinetic analyses of the CO_2 chemisorption mechanism on Na_2TiO_3: experimental and theoretical evidences, J. Phys. Chem. C 118 (2014) 19822–19832, http://dx.doi.org/10.1021/jp504922e.
[15] J.S. Lee, C.T. Yavuz, Enhanced sorption cycle stability and kinetics of CO_2 on lithium silicates using the lithium ion channeling effect of TiO_2 nanotubes, Ind. Eng. Chem. Res. 56 (2017) 3413–3417, http://dx.doi.org/10.1021/acs.iecr.6b04918.
[16] Q. Zheng, L. Huang, Y. Zhang, J. Wang, C.-Z. Zhao, Q. Zhang, W. Zheng, D. Cao, D. O'Hare, Q. Wang, Unexpected highly reversible topotactic CO_2 sorption/desorption capacity for potassium dititanate, J. Mater. Chem. A. 4 (2016) 12889–12896, http://dx.doi.org/10.1039/C6TA04117E.
[17] K. Wang, Z. Yin, P. Zhao, Z. Zhou, Z. Su, J. Sun, Development of metallic element-stabilized Li_4SiO_4 sorbents for cyclic CO_2 capture, Int. J. Hydrogen Energy 42 (2017) 4224–4232, http://dx.doi.org/10.1016/j.ijhydene.2016.10.058.
[18] Q. Zhang, D. Peng, S. Zhang, Q. Ye, Y. Wu, Y. Ni, Behaviors and kinetic models analysis of Li_4SiO_4 under various CO_2 partial pressures, AIChE J. 63 (2017) 2153–2164, http://dx.doi.org/10.1002/aic.15627.
[19] X. Yang, W. Liu, J. Sun, Y. Hu, W. Wang, H. Chen, Y. Zhang, X. Li, M. Xu, Preparation of novel Li_4SiO_4 sorbents with superior performance at low CO_2 concentration, ChemSusChem 9 (2016) 1607–1613, http://dx.doi.org/10.1002/cssc.201501699.
[20] X. Yang, W. Liu, J. Sun, Y. Hu, W. Wang, H. Chen, Y. Zhang, X. Li, M. Xu, Alkali-doped lithium orthosilicate sorbents for carbon dioxide capture, ChemSusChem 9 (2016) 2480–2487, http://dx.doi.org/10.1002/cssc.201600737.
[21] C. Yuming, Z. Yongchun, Z. Junying, Z. Chuguang, Hydrogen production through CO_2sorption-enhanced methane steam reforming: comparison between different adsorbents, Sci China Technol. Sci. 54 (2011) 2999–3008, http://dx.doi.org/10.1007/s11431-011-4587-6.
[22] H.K. Rusten, E. Ochoa-Fernández, H. Lindborg, D. Chen, H.A. Jakobsen, Hydrogen

production by sorption-enhanced steam methane reforming using lithium oxides as CO_2-acceptor, Ind. Eng. Chem. Res. 46 (2007) 8729–8737, http://dx.doi.org/10.1021/ie070770k.
[23] M.H. Halabi, J.M. De Croon, J. Van Der Schaaf, P.D. Cobden, J.C. Schouten, Reactor modeling of sorption-enhanced autothermal reforming of methane. Part II: effect of operational parameters, Chem. Eng. J. 168 (2011) 883–888, http://dx.doi.org/10.1016/j.cej.2011.02.016.
[24] C. Wang, Y. Chen, Z. Cheng, X. Luo, L. Jia, M. Song, B. Jiang, B. Dou, Sorption-enhanced steam reforming of glycerol for hydrogen production over a NiO/$NiAl_2O_4$catalyst and Li_2ZrO_3-based sorbent, Energy Fuels 29 (2015) 7408–7418, http://dx.doi.org/10.1021/acs.energyfuels.5b01941.
[25] E. Vera, B. Alcántar-Vázquez, H. Pfeiffer, CO_2 chemisorption and evidence of the CO oxidation–chemisorption mechanisms on sodium cobaltate, Chem. Eng. J. 271 (2015) 106–113, http://dx.doi.org/10.1016/j.cej.2015.02.075.
[26] E. Vera, B. Alcántar-Vázquez, Y. Duan, H. Pfeiffer, Bifunctional application of sodium cobaltate as a catalyst and captor through CO oxidation and subsequent CO_2 chemisorption processes, RSC Adv. 6 (2016) 2162–2170, http://dx.doi.org/10.1039/C5RA22749F.
[27] P.V. Subha, B.N. Nair, P. Hareesh, A.P. Mohamed, T. Yamaguchi, K.G.K. Warrier, U.S. Hareesh, CO_2 absorption studies on mixed alkali orthosilicates containing rare-earth second-phase additives, J. Phys. Chem. C. 119 (2015) 5319–5326, http://dx.doi.org/10.1021/jp511908t.
[28] M. Xiang, Y. Zhang, M. Hong, S. Liu, Y. Zhang, H. Liu, C. Gu, CO_2 absorption properties of Ti- and Na-doped porous Li_4SiO_4 prepared by a sol–gel process, J. Mater. Sci. 50 (2015) 4698–4706, http://dx.doi.org/10.1007/s10853-015-9020-2.
[29] J. Ortiz-Landeros, C. Gómez-Yáñez, L.M. Palacios-Romero, E. Lima, H. Pfeiffer, Structural and thermochemical chemisorption of CO_2 on $Li_{4-x}(Si_{1-x}Al_x)O_4$ and $Li_{4-x}(Si_{1-x}V_x)O_4$solid solutions, J. Phys. Chem. A 116 (2012) 3163–3171, http://dx.doi.org/10.1021/jp3006298.
[30] S. Zhang, M.B.I. Chowdhury, Q. Zhang, H.I. de Lasa, Novel fluidizable K-doped HAc-Li_4SiO_4 sorbent for CO_2 capture preparation and characterization, Ind. Eng. Chem. Res. 55 (2016) 12524–12531, http://dx.doi.org/10.1021/acs.iecr.6b03746.
[31] X. Chen, Z. Xiong, Y. Qin, B. Gong, C. Tian, Y. Zhao, J. Zhang, C. Zheng, High-temperature CO_2 sorption by Ca-doped Li_4SiO_4 sorbents, Int. J. Hydrogen Energy 41 (2016) 13077–13085, http://dx.doi.org/10.1016/j.ijhydene.2016.05.267.
[32] H. Pfeiffer, C. Vázquez, V.H. Lara, P. Bosch, Thermal behavior and CO_2 absorption of $Li_{2-x}Na_xZrO_3$ solid solutions, Chem. Mater. 19 (2007) 922–926, http://dx.doi.org/10.1021/cm0623965.
[33] J. Chenavas, J.C. Joubert, M. Marezio, Low-spin → high-spin state transition in high pressure cobalt sesquioxide, Solid State Commun. 9 (1971) 1057–1060, http://dx.doi.org/10.1016/0038-1098(71)90462-5.
[34] L. Martínez-dlCruz, H. Pfeiffer, Microstructural thermal evolution of the Na_2CO_3 phase produced during a Na_2ZrO_3–CO_2 chemisorption process, J. Phys. Chem. C. 116 (2012) 9675–9680, http://dx.doi.org/10.1021/jp301917a.
[35] B. Alcántar-Vázquez, C. Diaz, I.C. Romero-Ibarra, E. Lima, H. Pfeiffer, Structural and CO_2 chemisorption analyses on $Na_2(Zr_{1-x}Al_x)O_3$ solid solutions, J. Phys. Chem. C 117 (2013) 16483–16491, http://dx.doi.org/10.1021/jp4053924.
[36] G.J. Shu, W.L. Lee, F.T. Huang, M.W. Chu, P.A. Lee, F.C. Chou, Oxygen non-stoichiometry and the origin of Na ion ordering in P2-Na_xCoO_2, Phys. Rev. B–Condens. Matter Mater. Phys. 82 (2010) 1–6, http://dx.doi.org/10.1103/PhysRevB.82.054106.
[37] C. Schneider, P. Schichtel, B. Mogwitz, R. Straubinger, A. Beyer, M. Rohnke, K. Volz, J. Janek, Thermomigration and Soret effect in Na_xCoO_2 as thermoelectric material: preparation and characterization of sodium cobaltate thin films, Phys. Status Solidi. 213 (2016) 1284–1295, http://dx.doi.org/10.1002/pssa.201532725.
[38] M. Thommes, K. Kaneko, A.V. Neimark, J.P. Olivier, F. Rodríguez-Reinoso, J. Rouquerol, K.S.W. Sing, Physisorption of gases, with special reference to the evaluation of surface area and pore size distribution (IUPAC technical report), Pure Appl. Chem. 87 (2015) 1051–1069, http://dx.doi.org/10.1515/pac-2014-1117.
[39] N.S. McIntyre, D.G. Zetaruk, X-ray photoelectron spectroscopic studies of iron oxides, Anal. Chem. 49 (1977) 1521–1529, http://dx.doi.org/10.1021/ac50019a016.
[40] H.A. Lara-García, E. Vera, J.A. Mendoza-Nieto, J.F. Gómez-García, Y. Duan, H. Pfeiffer, Bifunctional application of lithium ferrites (Li_5FeO_4 and $LiFeO_2$) during carbon monoxide (CO) oxidation and chemisorption processes. A catalytic, thermogravimetric and theoretical analysis, Chem. Eng. J. 327 (2017) 783–791, http://dx.doi.org/10.1016/j.cej.2017.06.135.
[41] J.F. Gomez-Garcia, H. Pfeiffer, Structural and CO_2 capture analyses of the $Li_{1+x}FeO_2$ ($0 \leq x \leq 0.3$) system: effect of different physicochemical conditions, RSC Adv. 6 (2016) 112040–112049, http://dx.doi.org/10.1039/C6RA23329E.
[42] H.A. Lara-García, H. Pfeiffer, High and efficient Li_2CuO_2-CO_2 chemisorption using different partial pressures and enhancement produced by the oxygen addition, Chem. Eng. J. 313 (2017) 1288–1294, http://dx.doi.org/10.1016/j.cej.2016.11.029.
[43] I. Alcérreca-Corte, E. Fregoso-Israel, H. Pfeiffer, CO_2 absorption on Na_2ZrO_3: a kinetic analysis of the chemisorption and diffusion processes, J. Phys. Chem. C. 112 (2008) 6520–6525, http://dx.doi.org/10.1021/jp710475g.
[44] W. Gao, T. Zhou, Q. Wang, Controlled synthesis of MgO with diverse basic sites and its CO_2 capture mechanism under different adsorption conditions, Chem. Eng. J. 336 (2018) 710–720, http://dx.doi.org/10.1016/j.cej.2017.12.025.